

MIT Open Access Articles

New approach to remote gas-phase chemical quantification: selected-band algorithm

The MIT Faculty has made this article openly available. **Please share** how this access benefits you. Your story matters.

Citation: Niu, Sidi, Steven E. Golowich, Vinay K. Ingle, and Dimitris G. Manolakis. "New Approach to Remote Gas-Phase Chemical Quantification: Selected-Band Algorithm." *Opt. Eng* 53, no. 2 (December 23, 2013): 021111. © 2014 Society of Photo-Optical Instrumentation Engineers

As Published: <http://dx.doi.org/10.1117/1.oe.53.2.021111>

Publisher: SPIE

Persistent URL: <http://hdl.handle.net/1721.1/86022>

Version: Final published version: final published article, as it appeared in a journal, conference proceedings, or other formally published context

Terms of Use: Article is made available in accordance with the publisher's policy and may be subject to US copyright law. Please refer to the publisher's site for terms of use.



Optical Engineering

SPIEDigitalLibrary.org/oe

New approach to remote gas-phase chemical quantification: selected-band algorithm

Sidi Niu
Steven E. Golowich
Vinay K. Ingle
Dimitris G. Manolakis



New approach to remote gas-phase chemical quantification: selected-band algorithm

Sidi Niu,^{a,*} Steven E. Golowich,^b Vinay K. Ingle,^a and Dimitris G. Manolakis^b

^aNortheastern University, 360 Huntington Avenue, Boston, Massachusetts 02115

^bMIT Lincoln Laboratory, 244 Wood Street, Lexington, Massachusetts 02420

Abstract. We propose an algorithm for standoff quantification of chemical vapor plumes from hyperspectral imagery. The approach is based on the observation that the quantification problem can be easily solved in each pixel with the use of just a single spectral band if the radiance of the pixel in the absence of the plume is known. This plume-absent radiance may, in turn, be recovered from the radiance of the subset of spectral bands in which the gas species is transparent. This “selected-band” algorithm is most effective when applied to gases with narrow spectral features, and are therefore transparent over many bands. We also demonstrate an iterative version that expands the range of applicability. Simulations show that the new algorithm attains the accuracy of existing nonlinear algorithms, while its computational efficiency is comparable to that of linear algorithms. © 2014 Society of Photo-Optical Instrumentation Engineers (SPIE) [DOI: 10.1117/1.OE.53.2.021111]

Keywords: hyperspectral imagery; chemical plume quantification; selected-band algorithm; background estimation.

Paper 131164SSP received Jul. 31, 2013; revised manuscript received Oct. 24, 2013; accepted for publication Nov. 22, 2013; published online Dec. 23, 2013.

1 Introduction

The quantification of chemical vapor plumes by remote long-wave infrared (LWIR) hyperspectral sensing is an established capability, but existing signal processing algorithms do not yet cover all scenarios of potential interest. Most current algorithms employ either linear or nonlinear regression, both of which are deficient in different ways. Linear algorithms are limited in their applicability to optically thin plumes, whereas nonlinear algorithms are typically computationally intensive. In this article, we present an algorithm that exploits the spectral structure of the data in a new way to obtain the performance of nonlinear regression while retaining the speed of linear algorithms.

We will abide by the common requirement that plume quantification must be performed without prior knowledge of the scene in the absence of the plume. In particular, the background radiance behind the plume is unobserved. However, imaging sensors typically collect a large number of pixels not containing a plume. These pixels can be used to construct a subspace that spans the space of possible background data. Such constructions are commonly used in hyperspectral processing; the novelty of our algorithm is the way in which this subspace is used.

If the plume is optically thin, linear regression is adequate to solve the quantification problem, although even this case is not straightforward. Two aspects that require consideration are the treatment of thermal contrast between the plume and the background, and the problem of the gas signature exhibiting similarity to the background basis vectors. An iterative method¹ has been reported to solve the first problem, while a principal vector elimination process² or an orthogonal filter approach³ can be applied to overcome the second. However, any linear approach will degrade as the plume thickness departs the linear regime.

Nonlinear regression algorithms⁴⁻⁷ are capable of quantifying optically thick plumes. However, such algorithms have their own set of drawbacks. In particular, they typically incur an extra computational burden as compared to linear algorithms, and the most efficient among them converge only to local minima.

The new algorithm that we propose exploits the structure of the LWIR gas signatures to avoid the deficiencies of both the linear and nonlinear regression approaches. A typical gas signature exhibits strong varying behavior across the LWIR region. The absorption coefficients at certain spectral bands are much larger than the other bands, which leaves spectral bands with relatively small absorptions suitable for background radiance estimation. By contrast, the radiance of most condensed-phase background materials varies slowly with wavelength. As a result, the subspace occupied by the background pixels in a typical image has very low dimensionality; typically 10 or fewer. In contrast, many times this number of bands are transparent to most chemical plumes. Therefore, the transparent spectral bands can be used to recover the entire background radiance spectrum, including those parts normally obscured by the gas signature. Once the background radiance in a plume-present pixel is estimated, the gas quantity may be recovered from a “single” band, usually the one in which the absorption is strongest. We refer to this two-step procedure as the “selected-band” (SB) algorithm. We have preserved the simplicity of linear regression during background estimation, while retaining the exponential relationship of Beer’s law in the second step.

The remainder of this article is organized as follows. In Sec. 2, we will describe the physical model of at-sensor radiance and then, in Sec. 3, derive a variant of the on-plume radiance representation which is used during the plume simulation process. In Sec. 4, the derivation of the SB algorithm is illustrated by a gas with a spectrally narrow signature. It is

*Address all correspondence to: Sidi Niu, E-mail: niusidi@gmail.com

then extended to an iterative version for gases with broader signatures. The experimental results are given in Sec. 5 and concluding remarks in Sec. 6.

2 Radiance Model

The physical basis for gas detection with passive infrared sensors can often be explained with a simplified radiative transfer model,^{5,8} as illustrated in Fig. 1, that treats the atmosphere as homogeneous in temperature and transmittance and assumes the chemical plume, if present, to be close to the background. All scattering effects are out of scope of this article and thus ignored. Other nonplume absorptive gases, like water vapor, CO₂, ozone, etc., are assumed spatially constant and their absorption effects are included in the atmospheric transmittance. In this model, the at-sensor radiance in the absence of plume, as a function of wavelength, is given by

$$L_{\text{off}}(\lambda) = \tau_a(\lambda)L_b(\lambda) + [1 - \tau_a(\lambda)]B(\lambda, T_a), \tag{1}$$

where the two terms represent background radiance modulated by the atmosphere and atmospheric radiance. In Eq. (1), $\tau_a(\lambda)$ is defined to be the atmospheric transmittance, T_a is the temperature of the atmosphere, $L_b(\lambda)$ is the background radiance, and $B(\lambda, T)$ is the Planck function evaluated at wavelength λ and temperature T .

The presence of a plume has two effects: it absorbs part of the radiation emitted by the background, and it emits its own radiation. The resulting radiance is subsequently attenuated by transmission through the atmosphere, and is given by

$$L_{\text{on}}(\lambda) = [1 - \tau_a(\lambda)]B(\lambda, T_a) + \tau_a(\lambda)\tau_p(\lambda)L_b(\lambda) + \tau_a(\lambda)[1 - \tau_p(\lambda)]B(\lambda, T_p), \tag{2}$$

where $\tau_p(\lambda)$ is the plume transmittance and T_p its temperature. In Eq. (2), the three terms represent the at-sensor radiance due to the atmosphere, the background radiance as modulated by the plume and atmosphere, and the plume radiance as modulated by the atmosphere.

By adding and subtracting the term $[1 - \tau_a(\lambda)]B(\lambda, T_a)\tau_p(\lambda)$ to the right-hand side of Eq. (2), we can rewrite the on-plume radiance as

$$L_{\text{on}}(\lambda) = \tau_p(\lambda)\{\tau_a(\lambda)L_b(\lambda) + [1 - \tau_a(\lambda)]B(\lambda, T_a)\} + [1 - \tau_p(\lambda)]\{\tau_a(\lambda)B(\lambda, T_p) + [1 - \tau_a(\lambda)]B(\lambda, T_a)\}. \tag{3}$$

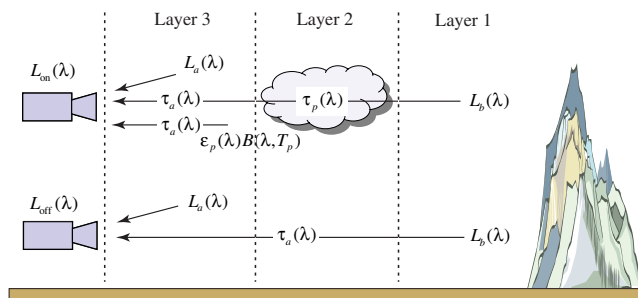


Fig. 1 Three-layer radiance model.

Comparison with Eq. (1) results in

$$L_{\text{on}}(\lambda) = \tau_p(\lambda)L_{\text{off}}(\lambda) + [1 - \tau_p(\lambda)] \times \{\tau_a(\lambda)B(\lambda, T_p) + [1 - \tau_a(\lambda)]B(\lambda, T_a)\}. \tag{4}$$

Equation (4) is the basis for embedding a simulated gaseous plume into a measured image of plume-free background data, as described in Sec. 3. Such simulated images will form the basis of the experiments reported in Sec. 5. This expression will also provide insight into why background estimation is achievable from on-plume radiance only.

The spectral transmission function, $\tau_p(\lambda)$, of a plume with M gas species can be modeled using Beer's law⁹

$$\tau_p(\lambda) = \exp\left[-\sum_{m=1}^M \gamma_m \alpha_m(\lambda)\right]. \tag{5}$$

The function, $\alpha_m(\lambda)$, the ‘‘absorption coefficient spectrum,’’ is unique for each gaseous chemical and can be used as a spectral signature. The quantity γ_m , the ‘‘concentration path-length (CL),’’ is the integrated concentration of gas along the sensor boresight. In this article, we will consider only the case of a plume comprising a single gas. As a result, we can drop the subscript m in Eq. (5) and rewrite Beer's law for a single gas as

$$\tau_p(\lambda) = \exp[-\gamma\alpha(\lambda)]. \tag{6}$$

3 Plume Simulation Process

The experiments of Sec. 5 will be performed using semi-synthetic data, in which the signatures of gaseous plumes are algorithmically embedded in measured hyperspectral imagery. This approach is taken both because controlled experiments with accurate ground truth on actual chemical releases are notoriously difficult, and arranging a large number of such experiments with a variety of conditions is infeasible. In this section, we describe the plume embedding algorithm.

3.1 Plume-Free Hyperspectral Imagery

The spectral mean image of a measured LWIR hyperspectral data is exhibited in Fig. 2.¹⁰ The data set was acquired in a down-looking geometry from an airborne platform, and the scene is composed mainly of natural materials. The spatial dimension of the testing data is 128 × 700 and there are 128 spectral bands from 7.3386 to 13.5703 μm. In this particular collection, sensor artifacts and noise rendered 43 of the spectral bands unsuitable for analysis. The remaining 85 bands are sufficient for the demonstrations of our algorithm that we discuss in Sec. 5. The whole field of view is free of any gaseous plume of interest and the radiance vector of

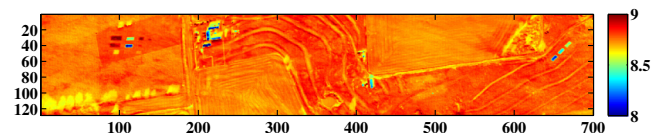


Fig. 2 Mean background radiance.

each pixel in Fig. 2 can be perceived as the off-plume radiance expressed in Eq. (1).

3.2 Gas Signature

In this article, two representative gases with very different characteristics are selected for subsequent algorithm derivation. Figure 3 illustrates the absorption coefficient spectrum of sulphur hexafluoride (SF_6), the absorption spectrum of which is mainly confined to a narrow spectral band. The high resolution library characterization¹¹ of the gas has been reduced to the sensor spectral resolution for easy comparison with other radiance figures in the article. As shown in the figure, the absorption coefficients of SF_6 in most of the spectral bands are almost zero. The other gas employed, triethyl phosphate (TEP), is absorbing in about half of the spectral bands, while the most absorptive band is only about a third as strong as that of SF_6 , as seen in Fig. 4. We expect quantification of the TEP-like gases to be more challenging than those with sharper features, since the TEP signature has some similarity to those of background materials.

3.3 Plume Simulation

The procedure of simulating a plume in measured background data is encapsulated by Eq. (4), which we rewrite as

$$L_{\text{on}}(\lambda) = \tau_p(\lambda)L_{\text{off}}(\lambda) + [1 - \tau_p(\lambda)]L_{\text{plume}}(\lambda), \quad (7)$$

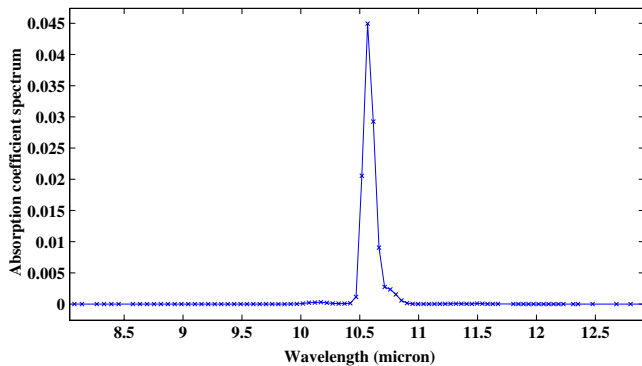


Fig. 3 Absorptive coefficient spectrum of SF_6 , smoothed and sampled at the sensor spectral resolution.

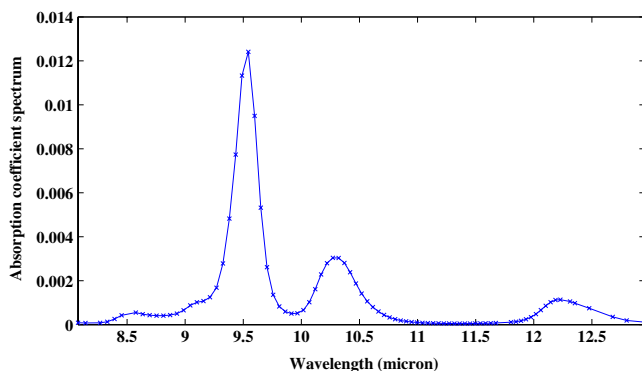


Fig. 4 Absorptive coefficient spectrum of triethyl phosphate (TEP), smoothed and sampled at the sensor spectral resolution.

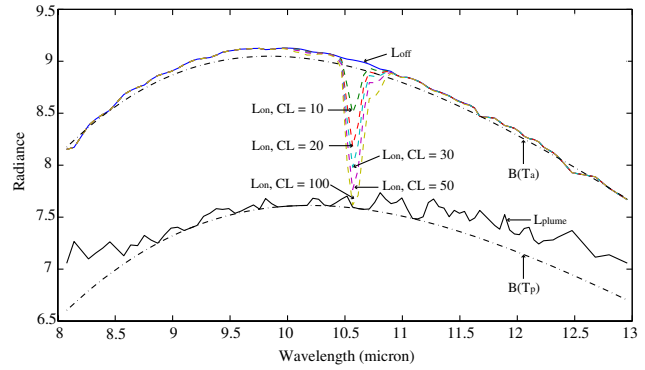


Fig. 5 Plume-free background radiance and corresponding on-plume radiances for SF_6 at five different thicknesses. The plume temperature is fixed at $T_p = T_a - 10$ K.

where the at-sensor plume radiance

$$L_{\text{plume}}(\lambda) = \tau_a(\lambda)B(\lambda, T_p) + [1 - \tau_a(\lambda)]B(\lambda, T_a) \quad (8)$$

is composed of two terms, the plume emission attenuated by atmosphere and the atmospheric path radiance. Since the gas quantity γ and gas absorption coefficient spectrum $\alpha(\lambda)$ are both non-negative, the range of transmittance defined by Beer's Law in Eq. (6) is confined between 0 and 1. As the plume thickens, its transmittance approaches zero. More background radiance is absorbed by the plume and the at-sensor radiance is then dominated by plume radiation. As a consequence, the on-plume radiance defined in Eq. (7) can be interpreted as a convex combination of off-plume radiance $L_{\text{off}}(\lambda)$ and at-sensor plume radiance $L_{\text{plume}}(\lambda)$.

During the embedding process, the temperature of the atmosphere, T_a , can be estimated from the data set and the atmospheric transmittance, $\tau_a(\lambda)$, can be obtained by auxiliary algorithms.¹⁰ These two atmospheric parameters are assumed constant over all pixels for each data cube. We may specify the location and temperature of a plume, as well as the amount of gas in each pixel. Figure 5 shows the radiance comparison between a randomly selected background pixel from Fig. 2 and its synthetic on-plume radiances with a sequence of different amounts of embedded SF_6 . For each sensor spectral band λ , the resulting on-plume radiance $L_{\text{on}}(\lambda)$ resides between $L_{\text{off}}(\lambda)$ and $L_{\text{plume}}(\lambda)$.

4 Selected-Band Algorithm

In this section, we will derive the SB algorithm by illustrating how to form accurate background radiance estimates. An iterative version of the algorithm is also proposed, which can achieve quantification of broadband gases. First, we emphasize why knowledge of the background radiance is sufficient for estimating the CL product.

All quantification algorithms discussed in this article, including our SB algorithms, assume that the plume temperature T_p , along with the atmospheric parameters T_a and $\tau_a(\lambda)$, are known, and we are interested in estimating the plume CL parameter γ . Therefore, in Eq. (7), $L_{\text{on}}(\lambda)$ and $L_{\text{plume}}(\lambda)$ are already available and CL estimation reduces to reversing Beer's law, Eq. (6), by

$$\gamma = \frac{1}{\alpha(\lambda)} \ln \left[\frac{L_{\text{off}}(\lambda) - L_{\text{plume}}(\lambda)}{L_{\text{on}}(\lambda) - L_{\text{plume}}(\lambda)} \right], \quad (9)$$

which holds for each λ . The remaining issues to address are estimating the only unknown quantity in Eq. (9), $L_{\text{off}}(\lambda)$, and the choice of band(s) to use in Eq. (9).

4.1 Background Radiance Representation

We follow many other authors^{1,12,2} in applying principal components analysis (PCA) to the plume-absent pixels in order to arrive at a representation of the background radiance of plume-present pixels. The plume-absent radiance, $L_{\text{off}}(\lambda)$, of plume-present pixels are assumed to lie in the subspace spanned by these principal vectors.

If we arrange the M_{off} off-plume measured radiance spectra into an $M_{\text{off}} \times K$ matrix \mathbf{L}_{off} , where K is the number of spectral bands, then the PCA model is given by

$$\mathbf{L}_{\text{off}} = \mathbf{U}\mathbf{P}^T + \mathbf{E}, \quad (10)$$

where \mathbf{U} is an $M_{\text{off}} \times N_p$ matrix of coefficients for off-plume pixels, \mathbf{P} is a $K \times N_p$ matrix of principal components, \mathbf{E} is an $M_{\text{off}} \times K$ matrix of residuals, and N_p is the number of principal components. For the data used in Sec. 5, we found $N_p = 5$ to be an appropriate choice. (The sum of variance from the first five principal vectors exceeds 99% of the total variance of the covariance matrix. With the particular data set shown in Fig. 2, $\sum_{i=1}^5 \sigma_i^2 / \sum_{i=1}^{85} \sigma_i^2 = 0.9956$, where σ_i^2 indicates the correspondent variance of the i 'th principal vector.) Data-adaptive algorithms can also be employed to find a suitable value for this parameter. In order to reduce ambiguity, we represent the plume-absent radiance L_{off} of plume-present pixels by l_{bkg} from now on. Assuming \mathbf{u} is a $1 \times N_p$ vector of unknown coefficients for the background radiance of an on-plume pixel

$$l_{\text{bkg}} = \mathbf{u}\mathbf{P}^T + \mathbf{e}, \quad (11)$$

the least-square estimate for \mathbf{u} is given by

$$\hat{\mathbf{u}} = l_{\text{bkg}} \mathbf{P}^{\dagger T} \quad (12)$$

where the Moore–Penrose pseudo-inverse is given by $\mathbf{P}^{\dagger} = (\mathbf{P}^T \mathbf{P})^{-1} \mathbf{P}^T$, and circumflex indicates an estimate. The background estimation task can now be rephrased as finding an accurate estimate $\hat{\mathbf{u}}$ when l_{bkg} is not available.

4.2 Algorithm Derivation

All existing algorithms assume that l_{bkg} is unobservable. However, if we inspect the radiance difference with and without the influence of a plume, shown in Fig. 5, we find the opposite. Suppose $\text{CL} = 30$ ppm-m, as shown in Fig. 6. The blue solid line represents the off-plume radiance of a randomly chosen background pixel whereas the red solid line corresponds to the simulated on-plume radiance of the same pixel. These two lines overlap each other over most of the spectrum and only differ in the few bands where the gas absorption coefficient is large. An implication is that the on-plume radiance is essentially equal to its background radiance over the most transparent spectral bands.

The spectral dimension of a typical hyperspectral sensor is at least on the order of 100 while a sufficient number of principal components N_p is typically < 10 . Hence, we can revise Eq. (12) by only selecting those bands where the

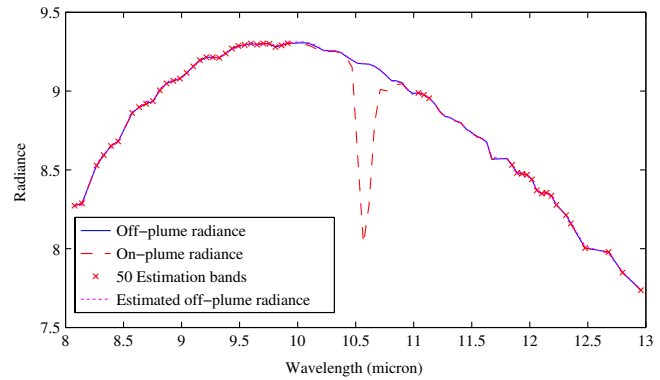


Fig. 6 Background radiance estimation process for a pixel with SF_6 embedded, with strength $\gamma = 30$ ppm-m. The plume temperature is fixed at $T_p = T_a - 10$ K.

gas absorption coefficient is almost zero. Thus, the least-square estimate for \mathbf{u} can be given by

$$\hat{\mathbf{u}} = l_{\text{on}}^{\text{sb}} \mathbf{P}^{\text{sb} \dagger T}, \quad (13)$$

where the superscript “sb” indicates only dimensions corresponding to SB are used. The background radiance at these bands can be substituted by the on-plume radiance $l_{\text{on}}^{\text{sb}}$.

The selection of which spectral bands are transparent enough to use in Eq. (13) is empirical, and we have adopted a very conservative strategy in our experiments. In Fig. 5, we observe that $\gamma = 100$ ppm-m is quite thick for SF_6 ; the most absorptive band is almost optically opaque. With such a thick plume present, the plume transmittance $\tau_p(\lambda)$ can be calculated and those bands with $\tau_p(\lambda) \geq 0.999$ are marked by red crosses in Fig. 6. In this case, 50 out of 85 spectral bands are selected, whereas, we have only $N_p = 5$ parameters to estimate. By solving Eq. (13) for the background radiance coefficient vector $\hat{\mathbf{u}}$ and substituting $\hat{\mathbf{u}}$ into Eq. (11), the background radiance is recovered and plotted as a dashed magenta line in Fig. 6. This estimate almost coincides over the entire spectrum with the true unobserved background radiance represented by the blue solid line.

With an accurate background radiance estimation in hand, we have K equations, one from each spectral band, to solve for only one variable in Eq. (9), the gas strength γ . However, most of these equations are inappropriate for this task. There are many sources of uncertainty on the right-hand side of Eq. (9): The on-plume radiance $L_{\text{on}}(\lambda)$ contains a noise contribution, the plume radiance $L_{\text{plume}}(\lambda)$ is affected by errors in the estimates of the atmospheric transmittance $\tau_a(\lambda)$ as well as those of the plume and atmosphere temperatures T_p and T_a , and the PCA expansion leaves some residual radiance in $L_{\text{off}}(\lambda)$. In the experiments we report in Sec. 5, it is the last of these sources that dominate the error in our CL estimates. Figure 7 illustrates the PCA representation mean error at each spectral band if $N_p = 5$. Since, the absorption coefficient is close to zero in many bands, even a small residual can result in highly inaccurate gas strength estimation at those bands. From Eq. (9), we may hypothesize that the most absorptive band will yield the smallest error in our CL estimates, which has been borne out in our simulations.

The block diagram of the proposed SB algorithm can be found in Fig. 8. In Fig. 9(a), the on-plume radiance and the

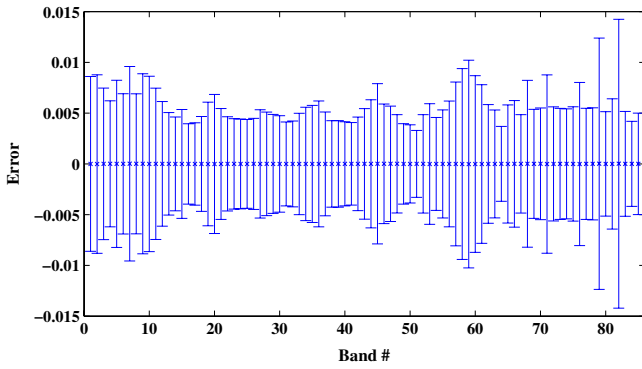


Fig. 7 Principal components analysis (PCA) representation error for radiance of off-plume pixels.

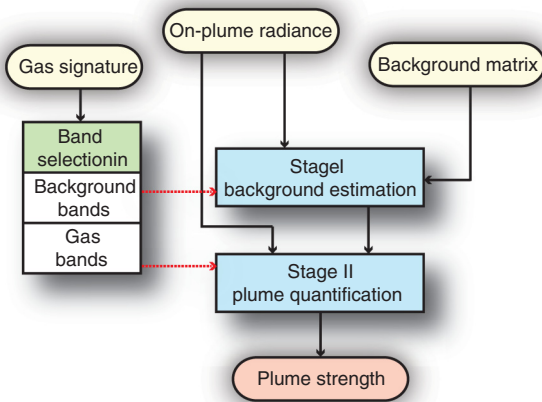
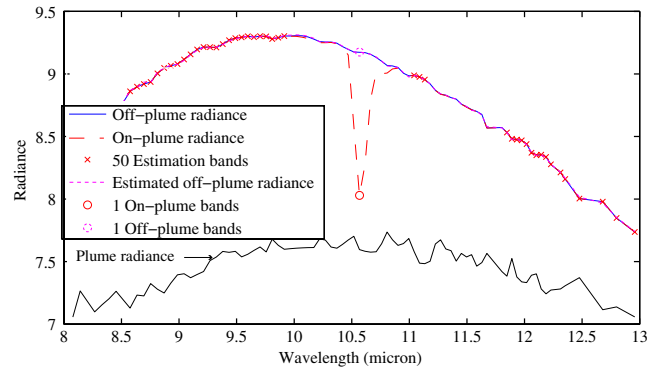


Fig. 8 Block diagram of selected-band (SB) algorithm.

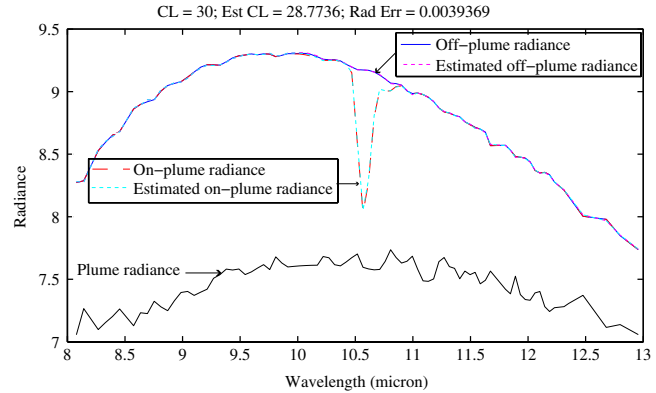
estimated background radiance are highlighted with a circle at the most absorptive band of SF₆. The gas strength is calculated from this spectral band with the results given in the title of Fig. 9(b). Also, shown in the figure, the recovered on-plume radiance (black dash line) coincides with the true on-plume radiance (red dash line) almost everywhere. The radiance difference between these two radiances is calculated and the result is given in the title as “Rad Err.” This result verifies that our estimates of background radiance and plume strength are both accurate.

One might ask if a least square solution of γ using multiple spectral bands can give improvements over the single-band result. In fact, such a procedure does not substantially reduce the error in the CL estimates, since the background radiance residuals over nearby bands are highly correlated due to the spectral smoothness of most natural background materials. We choose to use a single SB for the CL estimates throughout this article.

Although the SB algorithm works perfectly well when applied to narrow-band gases as SF₆, a problem arises when not enough near-to-zero spectral bands are available for background estimation when quantifying broad-band gases such as TEP. As shown in Fig. 10, there is noticeable disagreement between the off-plume and on-plume radiance. If we continue to use the same strict condition for transparency of absorption bands as we did for SF₆, <10 bands qualify, which are insufficient to compute an acceptable



(a)



(b)

Fig. 9 (a) Single most absorptive spectral band selected to estimate gas strength (b) plume strength estimation results and estimated on-plume radiance.

background estimate. A more forgiving threshold is necessary to obtain a sufficient number of spectral bands. In Fig. 10, if we choose the threshold to be 0.95, 44 spectral bands will be selected and the estimated background (magenta dashed line) is very close to the true one (blue solid line), though the radiance difference is noticeable in this case. Similar to the earlier SF₆ case, the most absorptive band is most robust to background representation error and thus returns the most reliable plume strength estimate. The estimation results are summarized in the title of Fig. 11, from which we observe that the plume strength estimate is

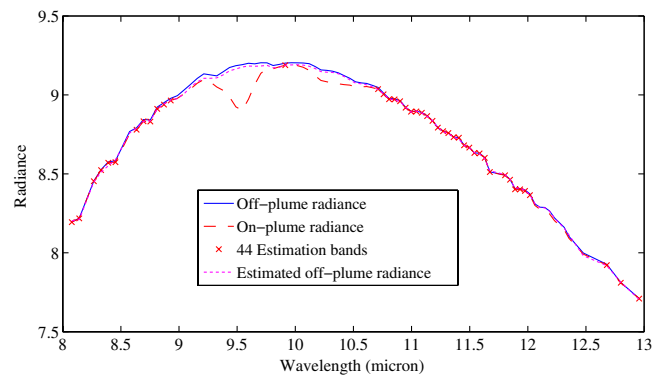


Fig. 10 Background radiance estimation process for a sample pixel when TEP of strength $\gamma = 30$ ppm-m is embedded. The plume temperature is chosen as $T_p = T_a - 10$ K.

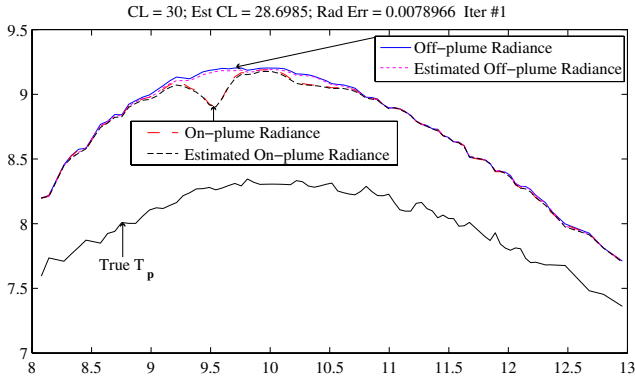


Fig. 11 Plume strength estimation results and estimated on-plume radiance.

acceptable while the recovered on-plume radiance error is somewhat large. Due to the broadband nature of gases like TEP, we are forced to incur some bias by choosing sufficiently many spectral bands. In the next section, we discuss a way to iteratively improve these estimates.

4.3 Performance Evaluation Metric

A necessary element of our iterative algorithm is a performance metric to optimize. Since the only data available in a real application is the on-plume radiance, we will use the radiance error to accomplish this task.

The on-plume radiance defined in Eq. (7) can be rewritten in vector form as

$$I_{on} = \tau_p \odot I_{off} + (1 - \tau_p) \odot I_{plume} \tag{14}$$

where \odot indicates the Hadamard product and all vectors are $1 \times K$ row vectors. For a given gas, the plume transmittance τ_p is determined by plume strength γ . According to Eq. (11), the off-plume radiance can be linearly approximated by a coefficient vector u . We define θ to represent all independent variables in Eq. (14), i.e., $\theta = \{u, \gamma\}$. Thus, a recovered on-plume radiance can be written explicitly as

$$I_{on}(\hat{\theta}) = \tau_p \odot I_{off} + (1 - \tau_p) \odot I_{plume} \tag{15}$$

Hence, we can compute the square root of squared radiance error as

$$Rad\ Err = \sqrt{[I_{on}(\hat{\theta}) - I_{on}(\theta)][I_{on}(\hat{\theta}) - I_{on}(\theta)]^T} \tag{16}$$

Strictly speaking, minimization of this performance evaluation metric on radiance error does not necessarily imply that the error in plume strength estimation is minimized. However, as far as our physical model is valid, a smaller radiance error generally results in better estimates of γ .

4.4 Iterative Version of the Algorithm

The performance evaluation metric from the previous section may be optimized in an iterative fashion; the block diagram of such an algorithm is given in Fig. 12. The initialization step is the same as the noniterative version of Sec. 4.2,

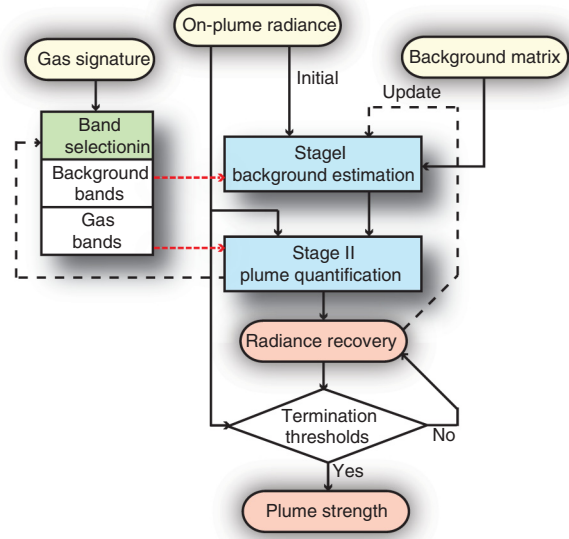


Fig. 12 Block diagram of iterative SB algorithm.

where the off-plume radiance is directly replaced by the observable on-plume radiance at the most transparent bands.

With the parameter estimation $\hat{\gamma}^i$ at iteration i at hand, it is trivial to compute the plume transmittance and solve for the background radiance. Figure 13 highlights the updated background estimate in 70 spectral bands at iteration two. The new recovered background radiance from the linear least square solution from these 70 equations is plotted as a magenta dashed line which overlaps the true background radiance (blue solid line) almost exactly. The new plume strength can then be calculated from the most absorptive band and its result (listed in the title of Fig. 14) is nearly identical to the true value. The updated recovered on-plume radiance is plotted by a black dashed line in Fig. 14, which is almost identical to the true radiance indicated by the red dash line. The radiance error listed in the title line is only about one fourth of previous iteration. The iterative method terminates if the improvement in radiance error is less than a preset threshold. In our experiments, we select this threshold to be 10% and the termination condition usually is satisfied within three iterations.

Figure 15 provides a graphical illustration of the improvement in estimates as the algorithm iterates. The blue line,

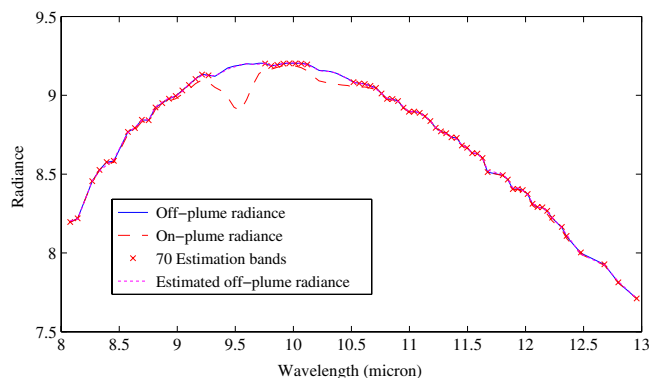


Fig. 13 Background radiance estimation.

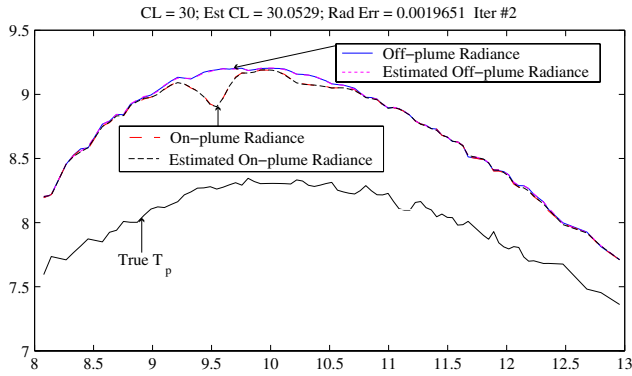


Fig. 14 Plume strength estimation results and estimated on-plume radiance.

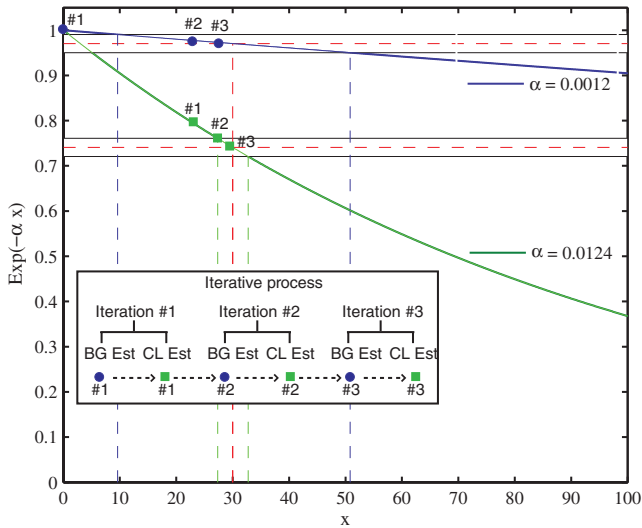


Fig. 15 Graphical illustration of iterative algorithm.

denoted by $\alpha = 0.0012$, represents the 20th most absorptive band of the TEP, which means 65 out of 85 spectral bands are less absorptive and used for background estimation. The green line, denoted by $\alpha = 0.0124$, is the most absorptive band and is used for quantification. The true gas strength and corresponding transmittance are highlighted with red dashed grid lines. The initialization step is denoted by a blue circle referred to as “#1.” In iteration 1, the background estimation stage leads to a biased estimate denoted by a green square referred to as “#1.” A gas strength estimate can be easily calculated from this biased estimate. In the next iteration, the plume strength estimate from the previous iteration can be used to recover the off-plume radiance, and the result is denoted by a blue circle referred to as “#2.” At this time, a more accurate background estimate can be achieved and thus a better estimate of gas strength is guaranteed. Empirically, the iterative method converges quite fast and fewer than three iterations is generally enough.

The success of iterative method relies on the high contrast of absorptive behavior between different bands. For the TEP, which has broader features than most gases, the most absorptive band is about 10 times as absorptive as the 20th most absorptive band. Since such sharp features are observed in almost all chemical gases, the applicability

of the iterative-version method is quite wide. Another benefit to the iterative algorithm is that the overall performance is less sensitive to band selection. In our experiments, similar performance was observed by choosing 60 to 80 spectral bands for background estimation.

5 Experimental Performance Comparison

In this section, we compare the quantification performance of our new SB algorithm with the other four state-of-the-art algorithms across a wide range of plume thicknesses. Three linear regression algorithms are implemented from Refs. 1–3, and their results will be denoted by final generalized least squares (GLSF), ordinary least squares (OLS), orthogonal background suppression (OBS), respectively. These algorithms all employ the linear approximation to Beer’s law and thus their performance deteriorates quickly as the gaseous plume thickens. The fourth algorithm, denoted by nonlinear least squares (NLS), uses an optimization method with its initial estimate from the result of a linear algorithm, so it can solve for the CL in the nonlinear least square sense.^{4,6,7} Detailed descriptions of our implementations of these algorithms can be found in our previous article.¹³ The performance of our new SB algorithm discussed in Sec. 4 will be denoted by SB.

5.1 Experiment Setup

All of the aforementioned algorithms are applied to simulated data. For each gas, there are two plume embedding schemes, one with a constant mask [red area in Fig. 16(a)] and the other with a Gaussian mask [colored area in Fig. 16(b)], as shown in Figs. 16(a) and 16(b), respectively. The constant mask is designed to investigate the quantification performance at a particular gas strength while the Gaussian mask is supposed to mimic a more realistic situation. The size of each mask is 21×41 . Pixels under the constant mask share the same CL value while CL is distributed normally under the Gaussian mask. For each mask profile, four experiments for each gas are performed: CL = 5, 10, 20, 30 ppm-m for SF₆ and CL = 10, 20, 30, 50 ppm-m for TEP. These CLs are selected so that both the linear and nonlinear regions are included. The temperature of plume is chosen to be $T_p = T_a - 10$ for all experiments.

5.2 Gas Strength Estimation Evaluation

In order to evaluate the CL estimation performance, we calculate the root mean square error of prediction (RMSEP) for each estimator, which is defined by

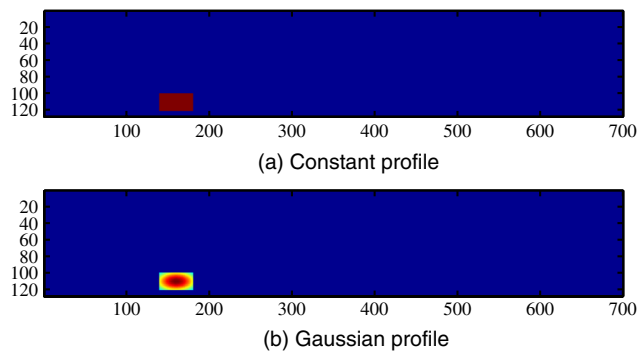


Fig. 16 21×41 embedding plume masks (a) constant profile (b) Gaussian profile.

$$RMSEP = \sqrt{\frac{1}{M_{on}} \sum_{j=1}^{M_{on}} (\hat{\gamma}_j - \gamma_j)^2}, \quad (17)$$

where M_{on} is the total number of on-plume pixels and $\hat{\gamma}_j$ indicates the estimated gas strength at pixel j .

5.3 Experimental Results

Figure 17 shows the background estimation performance for SF₆ when CL = 30 ppm-m with the constant embedding mask. In the figure, the blue symbols represent the mean and standard deviation of radiance error at each spectral band if the PCA coefficients are computed by the true background radiance. The red symbols denote the representation error by applying our SB background estimation approach to the on-plume radiance. We can see from the figure that our background estimation approach is very accurate and quite close to the optimal solution. The mean error of our estimates is <10% away from that of optimal solution. Figure 18 shows the background estimation performance for TEP when CL = 30 ppm-m with the constant mask. The estimation error is almost double that of SF₆. The results of the other experiments are similar.

The quantification results are shown in Figs. 19 and 20 for SF₆ and TEP, respectively. In Fig. 19, the three linear algorithms perform almost identically and as predicted the performance degrades rapidly as plume strength increases into the nonlinear regime. The nonlinear optimization algorithm

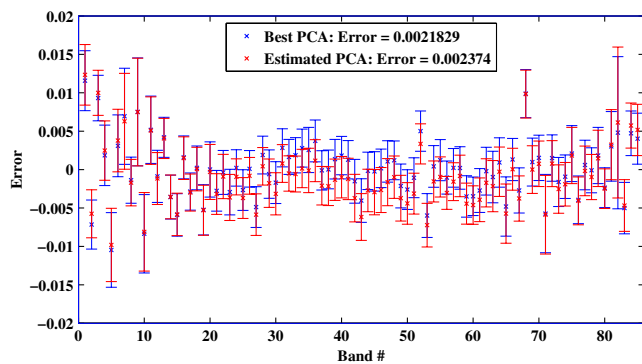


Fig. 17 The PCA representation error for background radiance of on-plume pixels with SF₆ embedded.

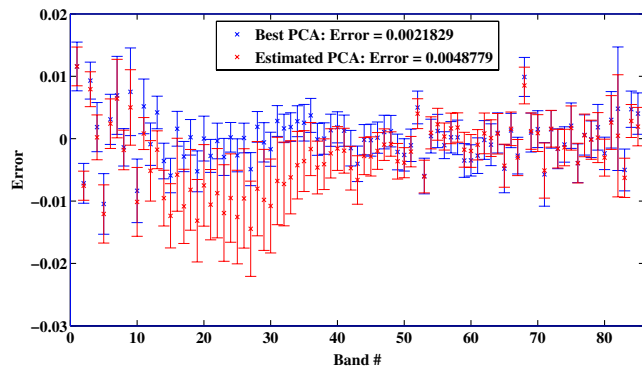
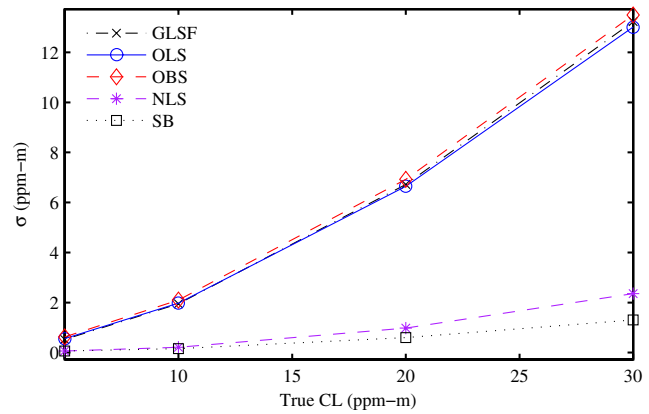
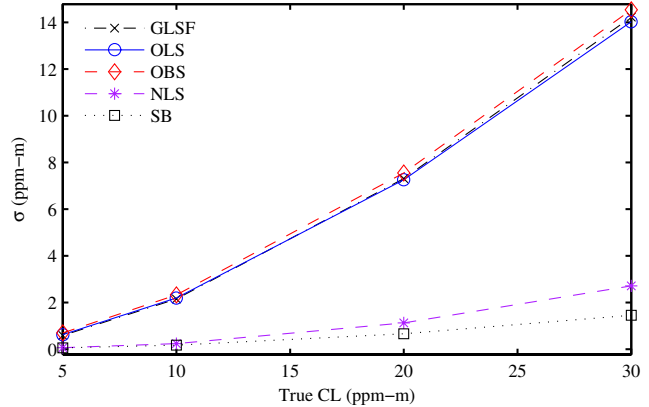


Fig. 18 The PCA representation error for background radiance of on-plume pixels with TEP embedded.



(a) Constant Mask



(b) Gaussian Mask

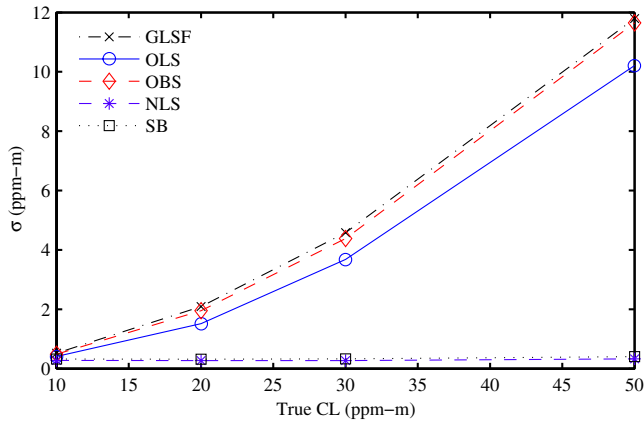
Fig. 19 Quantification performance comparison of SF₆ when $T_p = T_a - 10$ K with (a) constant profile and (b) Gaussian profile.

(purple dashed line with asterisk marker) is robust for all plume thicknesses but does not converge to a global minimum. Our SB algorithm (black dot line with square marker) outperforms all the other existing algorithms. Its estimation error only increases slightly as the plume gets thicker, which results from the curvature change in Beer's law.

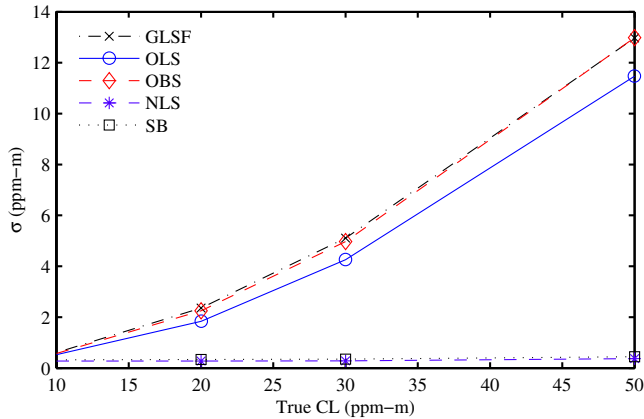
The performance comparison for TEP in Fig. 20 is similar. There are two issues worth mentioning. One is that the linear OLS outperforms the other two linear algorithms, which is because the OLS implementation employs a preprocessing procedure to exclude principal vectors, which are similar to the gas signature. This process is triggered for TEP and the fourth and fifth principal vectors are excluded. The other observation is that the performance of SB algorithm is visually identical to that of the optimization method. Both of these two algorithms are capable of consistently accurate estimation throughout all of TEP plume strengths.

If the result of SB algorithm is used to initialize the nonlinear optimization algorithm, the improvement in CL estimation is almost negligible, which confirms that our algorithm is capable of providing a near-to-optimal solution.

To verify that our results for TEP are typical, we also present results for tributyl phosphate (TBP), with the absorption spectrum plotted in Fig. 21. We specify the mean gas strength to be CL = 20, 30, 40, 50 ppm-m for the constant mask and maintain the plume temperature as $T_p = T_a - 10$. The performance comparison results are plotted in Fig. 22. The plot is similar to that of TEP as shown in



(a) Constant Mask



(b) Gaussian Mask

Fig. 20 Quantification performance comparison of the TEP with $T_p = T_a = 10$ K with (a) constant profile and (b) Gaussian profile.

Fig. 20(a) with the NLS performance slightly better than SB performance when the plume is extremely thin.

The computational complexity of each quantification algorithm is compared in Fig. 23. Each horizontal bar represents the overall execution time required to quantify $21 \times 41 = 861$ pixels by the corresponding quantification algorithm. The execution time is based on an Apple®, Cupertino, California MacBook Pro laptop with a 2.53 GHz Intel® Core 2 Duo processor. As shown in Fig. 23, the OBS is the most efficient, while OLS requires a little more time due to an extra principal vector elimination process.² The

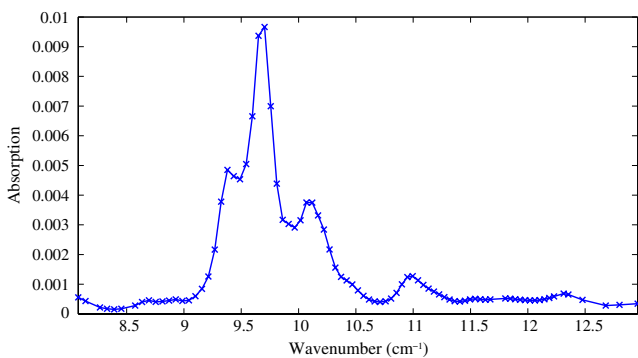


Fig. 21 Absorptive coefficient spectrum of tributyl phosphate (TBP), smoothed and sampled at the sensor spectral resolution.

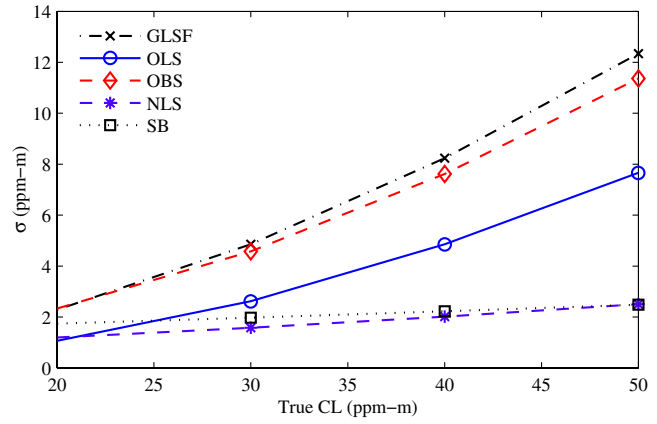


Fig. 22 Quantification performance comparison of the TBP with $T_p = T_a = 10$ K with constant profile.

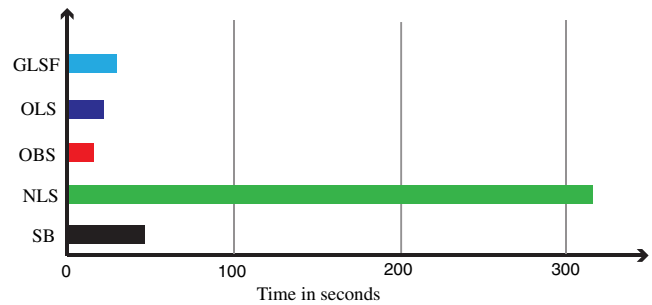


Fig. 23 Quantification algorithms execution time comparison.

GLSF is the most time consuming linear algorithm due to its iterative nature.¹ There is a large increase in execution time with the nonlinear least squares method, because at each iteration, a plume simulation process is called. In our implementation, this process requires calculation at a high frequency resolution (that of the gas library signature instead of sensor frequency resolution). A typical pixel usually takes 10 to 20 iterations before achieving its convergence. Our SB algorithm also requires this plume simulation process. However, since our algorithm converges within three iterations for most pixels, it achieves a significant saving in computational complexity, leaving its efficiency comparable to that of linear algorithms.

6 Conclusion

In this article, we proposed a new “SB” gas-phase chemical quantification algorithm, which is based on the realization that the background behind a chemical plume can be accurately estimated using only the spectral bands at which the plume is less absorptive. Once the background radiance is recovered, the spectral bands in which the gas absorbs significantly are used for gas strength estimation. The success of the algorithm relies on the large dynamic range of vapor-phase chemical absorptive coefficients. By separating the quantification process into two steps, the algorithm is able to achieve the efficiency of linear regression, as well as the wide applicability and accuracy of nonlinear approaches. Experimental results with semi-synthetic data verify that the quantification results of our new algorithm are as accurate as existing nonlinear algorithms but with an affordable increase in execution time compared to linear algorithms.

Acknowledgments

This work is sponsored by Defense Threat Reduction Agency (DTRA) Joint Science and Technology Office—Chemical and Biological Defense (JSTO-CBD) program, under Air Force Contract FA8721-05-C-0002. Opinions, interpretations, conclusions, and recommendations are those of the authors and not necessarily endorsed by the United States Government.

References

1. N. B. Gallagher, B. M. Wise, and D. M. Sheen, "Estimation of trace vapor concentration-pathlength in plumes for remote sensing applications from hyperspectral images," *Anal. Chim. Acta* **490**(1–2), 139–152 (2003).
2. S. J. Young, "Detection and quantification of gases in industrial-stack plumes using thermal-infrared hyperspectral imaging," Tech. Rep. ATR-2002(8407)-1, The Aerospace Corporation (2002).
3. A. F. Hayden and R. J. Noll, "Remote trace gas quantification using thermal IR spectroscopy and digital filtering based on principal components of background scene clutter," *Proc. SPIE* **3071**, 158–168 (1997).
4. C. M. Gittins, "Detection and characterization of chemical vapor fugitive emission by nonlinear optimal estimation: theory and simulation," *Appl. Opt.* **48**(23), 4545–4561 (2009).
5. T. Burr and N. Hengartner, "Overview of physical models and statistical approaches for weak gaseous plume detection using passive infrared hyperspectral imagery," *Sensors* **6**(12), 1721–1750 (2006).
6. R. Harig, G. Matz, and P. Rusch, "Scanning infrared remote sensing system for identification, visualization, and quantification of airborne pollutants," *Proc. SPIE* **4574**, 83–94 (2002).
7. P. Tremblay et al., "Standoff gas identification and quantification from turbulent stack plumes with an imaging fourier-transform spectrometer," *Proc. SPIE* **7673**, 76730H (2010).
8. D. F. Flanagan, "Prediction of the limits of detection of hazardous vapors by passive infrared with the use of modtran," *Appl. Opt.* **35**(30), 6090–6098 (1996).
9. G. E. Thomas and K. Stamnes, *Radiative Transfer in the Atmosphere and Ocean*, Cambridge University Press, Cambridge, UK (2002).
10. S. J. Young, B. R. Johnson, and J. A. Hackwell, "An in-scene method for atmospheric compensation of thermal hyperspectral data," *J. Geophys. Res.: Atmos.* **107**(D24), ACH 14-1–ACH 14-20 (2002).
11. S. W. Sharpe et al., "Gas-phase databases for quantitative infrared spectroscopy," *Appl. Spectrosc.* **58**(12), 1452–1461 (2004).
12. A. Hayden, E. Niple, and B. Boyce, "Determination of trace-gas amounts in plumes by the use of orthogonal digital filtering of thermal-emission spectra," *Appl. Opt.* **35**(16), 2802–2809 (1996).
13. S. Niu et al., "Algorithms for remote quantification of chemical plumes: a comparative study," *Proc. SPIE* **8390**, 83902I (2012).

Sidi Niu is currently a PhD candidate and research assistant in the Department of Electrical and Computer Engineering at Northeastern University. His research interests include hyperspectral image processing, remote sensing, digital image processing, pattern recognition, and computer vision. He received his MS from Northeastern University and BS from Zhejiang University, China, both in electrical engineering.

Steven Golowich is a technical staff member at MIT Lincoln Laboratory, where his research interests include signal processing, remote sensing, and structured light. He was awarded a PhD in physics by Harvard University and an A.B. in physics and mathematics by Cornell University. Previously, he was a member of technical staff at the Bell Labs Math Center, and taught at Princeton University. He received the American Statistical Association Outstanding Application award and the Wilcoxon Prize.

Vinay K. Ingle is currently an associate professor in the Department of Electrical and Computer Engineering at Northeastern University. He has taught courses in systems, signal/image processing, communications, and control theory. He has co-authored several textbooks on signal processing including digital signal processing using MATLAB (Cengage, 2012), applied digital signal processing (Cambridge University Press, 2011), and statistical and adaptive signal processing (Artech House, 2005). He is actively involved in hyperspectral imaging and signal processing.

Dimitris Manolakis is currently a senior member of the technical staff at MIT Lincoln Laboratory. He is coauthor of the textbooks Digital Signal Processing: Principles, Algorithms, and Applications (Prentice-Hall, 2006, 4th ed.), Statistical and Adaptive Signal Processing (Artech House, 2005), and applied Digital Signal Processing (Cambridge University Press, 2011). His research experience and interests include the areas of digital signal processing, adaptive filtering, array processing, pattern recognition, remote sensing, and radar systems.